Front. Earth Sci. 2016, 10(3): 409–418
DOI 10.1007/s11707-016-0579-y

RESEARCH ARTICLE

A case study of GOES-15 imager bias characterization with a numerical weather prediction model

Lu REN (✉)

Department of Climate and Space Sciences and Engineering, University of Michigan, MI 48109, USA

Abstract The infrared imager onboard the Geostationary Operational Environmental Satellite 15 (GOES-15) provides temporally continuous observations over a limited spatial domain. To quantify bias of the GOES-15 imager, observations from four infrared channels (2, 3, 4, and 6) are compared with simulations from the numerical weather prediction model and radiative transfer model. One-day clear-sky infrared observations from the GOES-15 imager over an oceanic domain during nighttime are selected. Two datasets, Global Forecast System (GFS) analysis and ERA-Interim reanalysis, are used as inputs to the radiative transfer model. The results show that magnitudes of biases for the GOES-15 surface channels are approximately 1 K using two datasets, whereas the magnitude of bias for the GOES-15 water vapor channel can reach 5.5 K using the GFS dataset and 2.5 K using the ERA dataset. The GOES-15 surface channels show positive dependencies on scene temperature, whereas the water vapor channel has a weak dependence on scene temperature. The strong dependence of bias on sensor zenith angle for the GOES-15 water vapor channel using GFS analysis implies large biases might exist in GFS water vapor profiles.

Keywords data assimilation, NWP, GOES imager, bias

1 Introduction

The second generation of Geostationary Operational Environmental Satellites (GOES-7 through GOES-15) provides nearly time-continuous radiance measurements over their observation domains with high spatial resolution. Recently, use of GOES imager radiance has been extended not only for retrieval of atmospheric variables, but also to direct radiance assimilation in data assimilation systems. Development of direct assimilation of imager radiance from geostationary satellites lags behind the assimilation of radiance measurements from polar-orbiting satellites. Preliminary studies of the assimilation of geostationary imager radiance include Köpken et al. (2004) for the Meteosat Visible and Infrared Imager (MVIRI) onboard Meteosat-7 and Szyndel et al. (2005) for the Spinning Enhanced Visible and Infrared Imager (SEVIRI) onboard Meteosat-8. Su et al. (2003) assimilated GOES imager radiance in the global data assimilation system and found a slight degradation. In a previous study, the potential benefits of assimilating GOES imager radiance in the data assimilation system for coastal quantitative precipitation forecasts (QPFs) (Qin et al., 2013) was investigated. In that study, a data-thinning scheme was applied to alleviate the strong correlation between nearby observations.

Since the data assimilation system is designed to remove only random error (Dee, 2005), bias characterization is critical for effectively using satellite observations; otherwise, the bias of any instrument could impair the model forecast over an extremely short timespan (Auligné et al, 2007). This study assesses the instrumental bias of the infrared imager onboard the last flight unit of the GOES second-generation program (GOES-15 located at 135°W), using numerical weather prediction (NWP) background fields and a radiative transfer model under clear-sky conditions. A single-period dataset from the GOES-15 imager is evaluated, rather than a dataset spanning over an extended period. Even though the global bias characterization was completed, the impact of assimilating the imager was neutral or slightly negative. Therefore, it is necessary to check on potential problems regionally. This article is organized as follows. Section 2 introduces instrument characteristics of the GOES-15 imager. The procedure that converts the instrument output (e.g., raw count) to the physical quantities (e.g., brightness temperature) is presented in Section 3. The model simulation of GOES-15 imager brightness temperature is introduced in Section 4. A detailed configuration of the case study and related discussion is given in Section 5. Conclusions are presented in Section 6.

Received August 29, 2015; accepted December 30, 2015

E-mail: lren@umich.edu

2 Instrument characteristics of GOES-15 imager

The GOES-15 satellite has operated successfully since 6 December 2011 at 135°W. The imager onboard GOES-15 has five channels (1, 2, 3, 4, and 6). The central wavelengths of these channels are respectively 0.65 μm, 3.9 μm, 6.5 μm, 10.7 μm, and 13.3 μm. Since GOES-12, the original channel 5 with the central wavelength of 12.0 μm was replaced with the 13.3 μm channel, located at the wing of a CO_2 absorption band. The field of view (FOV) of the visible and infrared channels was 28 μrad and 112 μrad, respectively, with a corresponding nadir spatial resolution of approximately 1 km and 4 km. The maximum coverage of the GOES-15 imager is shown in Fig. 1.

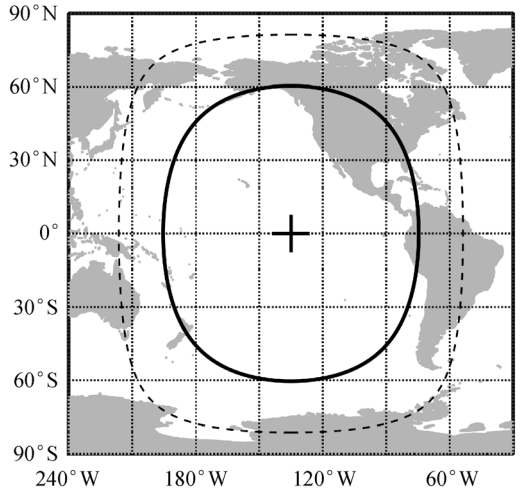

Fig. 1 The maximum coverage (dashed) and the coverage with the pixel distortion index less than 3 (solid) of GOES-15 imager in 2012. The sub-satellite point is at 135°W.

Since the imager scans in a manner similar to that of cross-track sensors, the area of each FOV on the earth surface is distorted. Pixel distortion index K can be used to assess one-dimensional distortion through the following equation (Capderou, 2005; Da and Zou, 2014):

$$K = \frac{a}{h} \cdot \frac{\sin^2\alpha + (\cos\alpha - \cos\alpha_0)^2}{\cos\alpha - \cos\alpha_0}, \quad (1)$$

$$\alpha = |\lambda - \lambda_{nadir}|, \quad (2)$$

where λ_{nadir} and λ are the latitude or longitude of the satellite nadir and calculated pixel, respectively; a is the distance from the satellite to earth center, and h is the satellite height above earth's surface. It can be calculated that the pixel distorts three times over the area at nadir at a latitude of approximately 60°.

If the scattering process is neglected, the radiance received by the imager during nighttime consists of two components. The first comes from the transmitted radiance from the Earth's surface to the top of the atmosphere. The second accounts for the transmitted radiance by each atmospheric layer. The atmospheric contribution is described by a physical variable called the weighting function (Fig. 2). It is seen that while channel 2, 4, and 6 are more sensitive to the surface, the weighting function peak of channel 3 is located at about 300–500 mb.

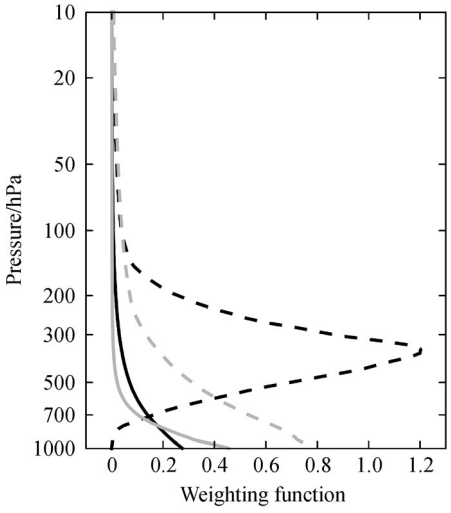

Fig. 2 Weighting functions (WFs) of the GOES-15 imager channels at 3.9 μm (black solid), 6.5 μm (black dashed), 10.7 μm (gray solid), and 13.3 μm (gray dashed), calculated by the Community Radiative Transfer Model (CRTM) based on the US standard atmosphere.

3 Conversion from counts to brightness temperature

The calibration involves conversion from raw input (e.g., digital counts) to physical variables (e.g., brightness temperature). During the observation period, the imager executed the cold space view, earth scene view, and warm target view. The cold space view refers to the scan that targets cold space with a constant temperature of 2.73 K. The warm target view is completed by viewing an internal blackbody inside the imager. Each type of view returns a digital count related to the current voltage. The detailed calibration process is described in Menzel et al. (1993), Weinreb et al. (1997), and Schmit et al. (2012). The calibration has three steps. First, the digital count c_v can be converted to observed radiance R_v at the central wavelength v through

$$R_v = a_v c_v + b_v, \quad (3)$$

where a_v and b_v are channel-dependent coefficients related to the warm counts, cold counts, and the temperature of both the cold space and the internal blackbody.

By inverting the Planck function, R_v can be converted

into the effective temperature T_v^{eff} through

$$T_v^{eff} = \frac{c_2 v}{\ln\left(\frac{c_1 v^3}{R_v} + 1\right)}, \quad (4)$$

where c_1 and c_2 are constants with values of 1.191066×10^{-5} mW/(m^2·sr·cm^{-4}) and 1.438833 K/(cm^{-1}), respectively.

Since the detector observes the target in a narrow band instead of a single wavelength in reality, a spectral correction is made to T_v^{eff} according to the spectral response function of the detector, via

$$T_v^b = aT_v^{eff} + \beta, \quad (5)$$

where α and β are detector- and band-dependent coefficients. T_v^b is the observed brightness temperature of the specific channel.

In this study, the raw counts data of the GOES-15 imager is downloaded from the NOAA Comprehensive Large Array-data Stewardship System (CLASS). The conversion coefficients used in Eqs. (3), (4), and (5) can be found at http://www.ospo.noaa.gov/Operations/GOES/calibration/gvar-conversion.html.

4 Model simulation of clear-sky brightness temperature

There are two common approaches to evaluate post-launch bias characteristics of an instrument onboard the satellite. The first performs inter-calibration of the new sensor with an existing well-calibrated sensor. For example, the imager onboard a geostationary satellite can be inter-calibrated with the hyperspectral infrared sounders onboard polar-orbiting satellites (Hewison et al., 2013). This approach can be used under all sky conditions. The disadvantage here is that it is difficult to perform the calibration over the full-disk observations of the imager. Given the different viewing geometry and the orbit height, it is necessary to impose several collocation criteria to ensure that the air masses over which the observations are collocated share similar properties. Another way to assess the post-launch bias involves the use of the NWP fields, such as temperature and water vapor profiles, and a radiative transfer model that transforms the physical variables from profile space to brightness temperature or radiance space. This method can be used to evaluate full-disk bias, but it also has some inadequacies. For example, it cannot separate instrument bias from background and forward model biases. In addition, although the model can simulate brightness temperature under cloudy conditions, it requires accurate input of hydrometeor properties, such as cloud top height and size distribution.

In the present study, the second approach is utilized to evaluate bias characteristics of the GOES-15 imager. The GFS analysis and ERA-Interim reanalysis serve as the background information. The GFS analysis has a spatial resolution of 0.5° with 26 vertical isobaric levels up to 10 hPa, whereas ERA-Interim reanalysis has a spatial resolution of 0.75° and 60 vertical model layers up to 0.1 hPa. The purpose for using two types of backgrounds is to determine the bias introduced by the background. Any patterns not shared by the two backgrounds are likely attributable to bias from the background instead of the instruments. Community Radiative Transfer Model (CRTM) (Han et al., 2007) version 2.1.3 serves as the radiative transfer model in this study. CRTM utilizes the advanced doubling and adding technique as a radiative transfer (RT) solver. For surface emissivity, it uses empirical database models over both land and ocean. To account for the sun-glint effect during daytime over the ocean, the sea surface is assumed to consist of numerous small facets and follows the Cox and Munk (1954) distribution function. For gas absorption, the fast Optical Path Transmittance algorithm is applied to calculate mass absorption by atmospheric gases. Since shortwave CO_2 bands at about 4.3 μm experience the non-local temperature equilibrium effect, a regression model is incorporated to alleviate this bias (Chen et al., 2013).

5 Case study at 0600UTC on 23 June 2012

As mentioned in Section 4, the calibration method using NWP fields and the RT model has two disadvantages. To alleviate their influences, several filtering processes are performed on the GOES-15 imager observations. First, the investigated region is located within 35°S−5°N, 125°W−100°W at 0600UTC over the ocean on 23 June 2012. This alleviates the ambiguity of the RT solution caused by surface emissivity and excludes interference from the solar radiation. Second, cloudy imager pixels are removed so that only clear-sky pixels will be used to assess instrument bias. This avoids bias caused by the incorrect assignment of clouds. To do so, the GOES-15 imager observations are collocated with MODIS Level-2 cloud fraction, at a resolution of 5 km at nadir (Fig. 3). The converted brightness temperature of the GOES-15 imager from the raw counts of the same region is shown in Figs. 4 and 5. The collocation criteria include a maximum temporal difference of 5 minutes and a maximum spatial difference of 2 km. Only imager pixels with a cloud fraction less than 1% are used. Third, pixels with a sensor zenith angle greater than 60° are excluded to avoid strong variation of air mass properties. Finally, 48,642 GOES imager pixels remained for the bias calculation. It is seen that the pixels are mainly distributed over the sensor zenith angle ranging from 10° to 50° (Fig. 6).

As shown by Da (2015), the mean and standard

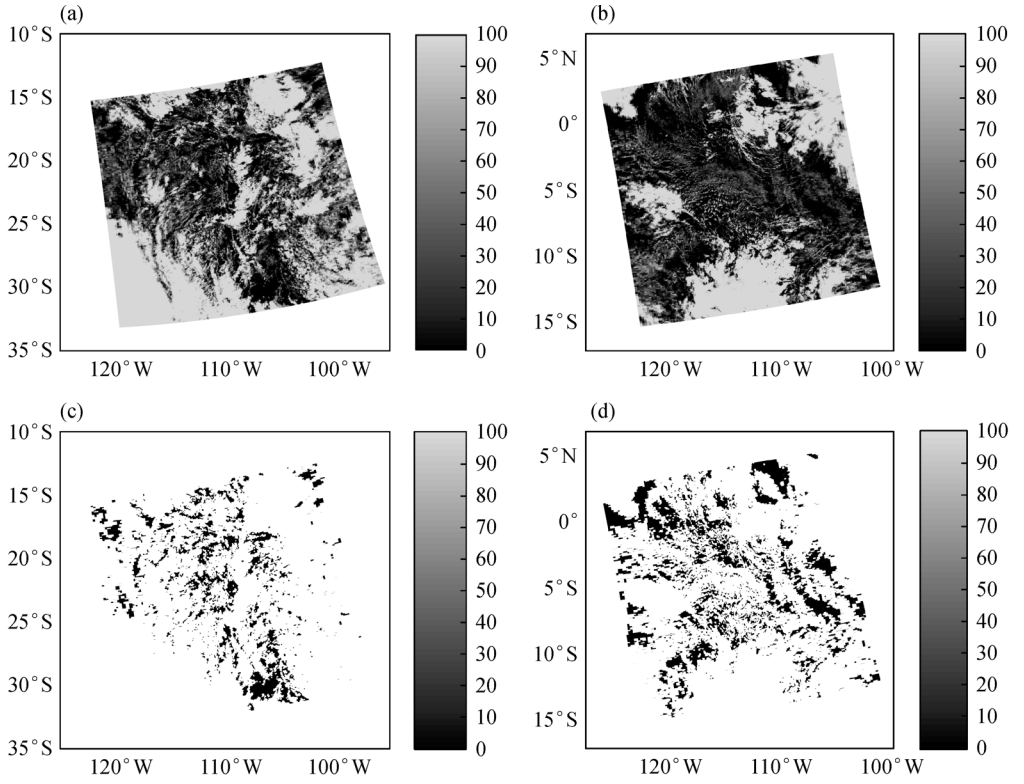

Fig. 3 Cloud fraction based on MODIS Level 2 cloud products at (a) 0600UTC, June 23, 2012, and (b) 0605UTC, June 23, 2012. The corresponding pixels with $f^{cld} < 10\%$ are respectively shown in (c) and (d).

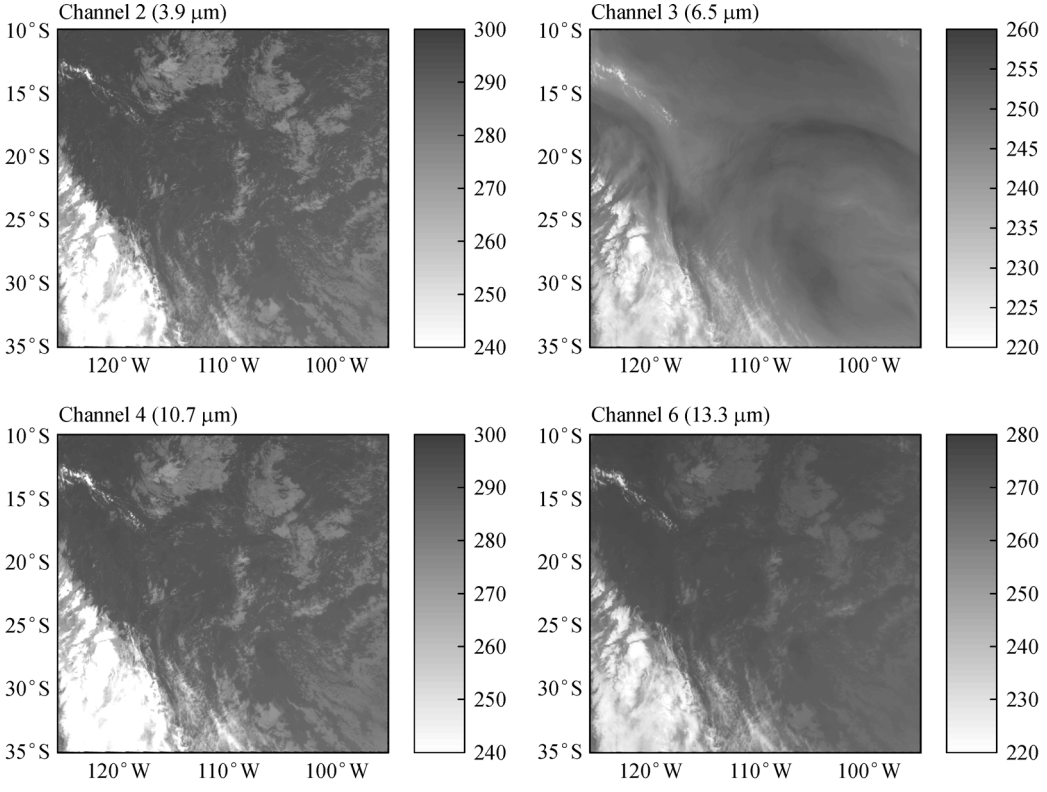

Fig. 4 The observed brightness temperature of GOES-15 imager channels 2, 3, 4, and 6 over the same region covered by MODIS in Fig. 3(a).

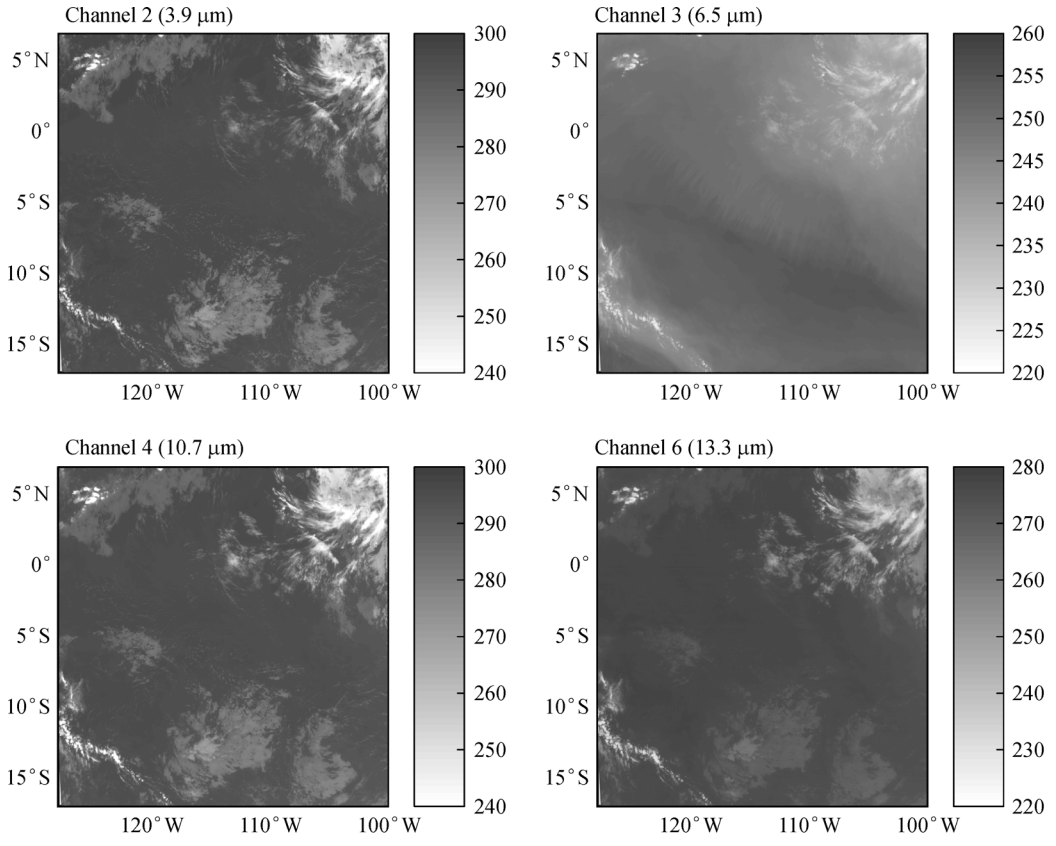

Fig. 5 The observed brightness temperature of GOES-15 imager channels 2, 3, 4, and 6 over the same region covered by MODIS in Fig. 3(b).

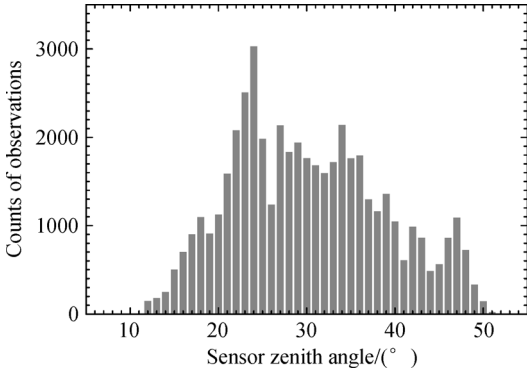

Fig. 6 The histogram of the collocated GOES-15 imager clear-sky pixels with different sensor zenith angles (48,642 pixels total).

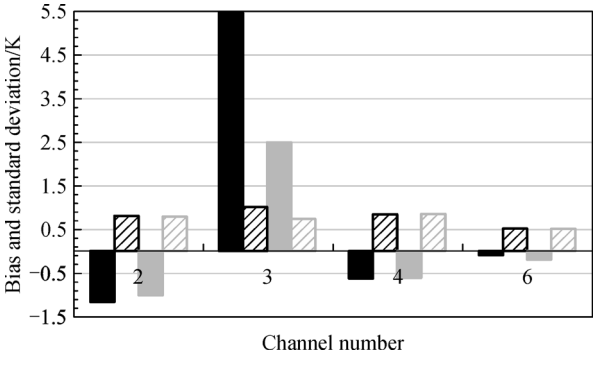

Fig. 7 The bias (solid) and standard deviation (dashed) of $(T_b^{obs} - T_b^{sim})$ (Unit: K) for GOES-15 channels 2, 3, 4, and 6 when using the GFS analysis (black) or the ERA-Interim reanalysis (grey) as the background.

deviation of $T_b^{obs} - T_b^{sim}$ represent two key parameters (bias and error covariance) in the data assimilation system. The calculated mean and standard deviation of $T_b^{obs} - T_b^{sim}$ are shown in Fig. 7.

Biases are within 1.0 K for surface channels 2, 4, and 6. For the water vapor channel, the bias is close to 5.5 K using the GFS as background and 2.5 K using ERA-Interim reanalysis as background. This large difference may indicate biases existing in either the background or the forward model. One indication that the background bias may play a role here is that the bias using ERA-Interim reanalysis, with 47 layers below 10 hPa, is smaller than that using GFS analysis, with 26 layers below 10 hPa. For the standard deviation of the combined error, the ERA-Interim reanalysis and GFS analysis are quite consistent. All four channels have errors below 1.0 K. Another thing worth noticing is that all surface channels have negative

biases. This may indicate that pixels contaminated by clouds are not completely removed. It can be observed from Fig. 8 that for all the imager channels, $T_b^{obs} - T_b^{sim}$ has relatively long tails on the negative value side. Overall, they all share a shape similar to that of a Gaussian.

The dependence of bias on scene temperature was also

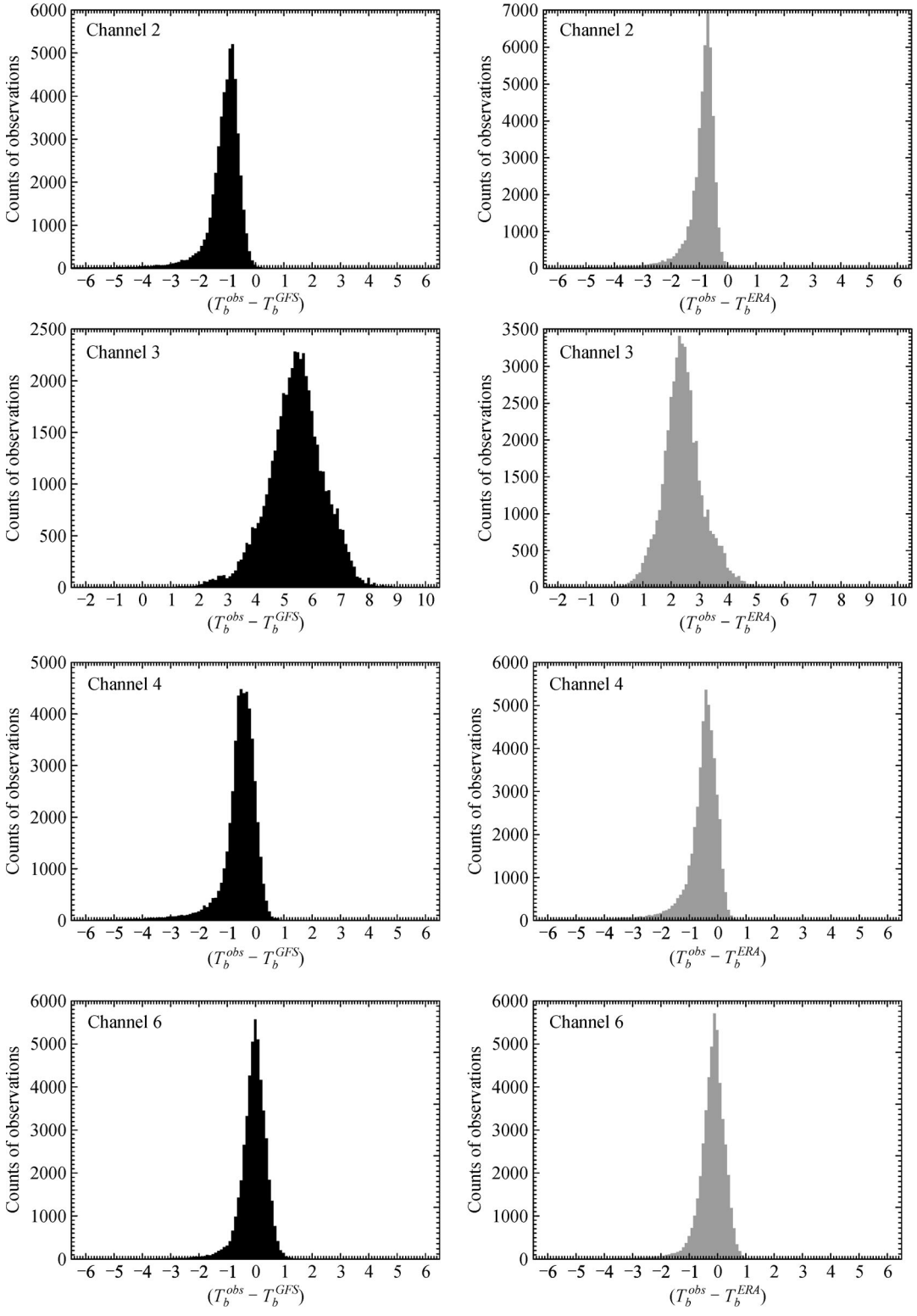

Fig. 8 The histogram of $(T_b^{obs} - T_b^{sim})$ (Unit: K) for GOES-15 channels 2, 3, 4, and 6 if using the GFS analysis (black) or the ERA-Interim reanalysis (grey) as the background.

investigated. A well-calibrated sensor should not have scene-dependent biases. In other words, $T_b^{obs} - T_b^{sim}$ should show no dependence on the observed brightness temperature T_b^{obs}. However, for both the GFS and ERA-Interim backgrounds (Figs. 9 and 10), bias for three surface channels (channels 2, 4, and 6) shows positive dependence on scene temperature. The dependence is not obvious for the water vapor channel.

Since the GOES imager onboard GOES-15 scans the earth in a similar manner to that of the cross-track sensor, it is necessary to check whether the bias has scan-angle dependence due to the limb effect. It can be easily shown that the scan angle and the sensor zenith angle are strongly correlated. Thus, for convenience, the dependence of bias on sensor zenith angle is directly explored (Figs. 11 and 12).

It is interesting that the bias shows no obvious dependence on sensor zenith angle for the surface channels, unlike the cross-track sensor onboard polar-orbiting satellites. One explanation for this is that the geostationary satellite is far from the earth surface, when comparing the satellite altitude of 25,786 km with the earth radius of 6371 km. The variation of the optical depth due to the scan angle is small. Another notable feature is the strong dependence of the bias on sensor zenith angle for the water vapor channel using the GFS as background; a feature that is not seen when using ERA-Interim as the background. This pattern implies there are large biases in GFS water vapor profiles. It is worth mentioning that bias of the GOES-15 water vapor channel varies dramatically with space and time due to the high variability of the water vapor. The long-time bias statistics might underestimate this error and lead to an inaccurate bias correction for that channel. The best solution is to improve the performance of forecast models internally rather than characterizing the bias of the GOES-15 water vapor channel externally.

6 Summary and conclusions

The infrared imager onboard the GOES-15 satellite has four infrared channels. Channels 2, 4, and 6 are sensitive to the surface, whereas channel 3 is sensitive to water vapor in the troposphere. Given the data assimilation system requires the biases of satellite observations be properly removed, the four infrared channels from the GOES imager are compared with simulations from the CRTM. In this study, one-day infrared observations from the GOES-15 imager over an oceanic domain during nighttime are first converted from digital counts to brightness temperatures. Cloudy pixels are then removed by collocating GOES-15 observations with MODIS Level 2 cloud

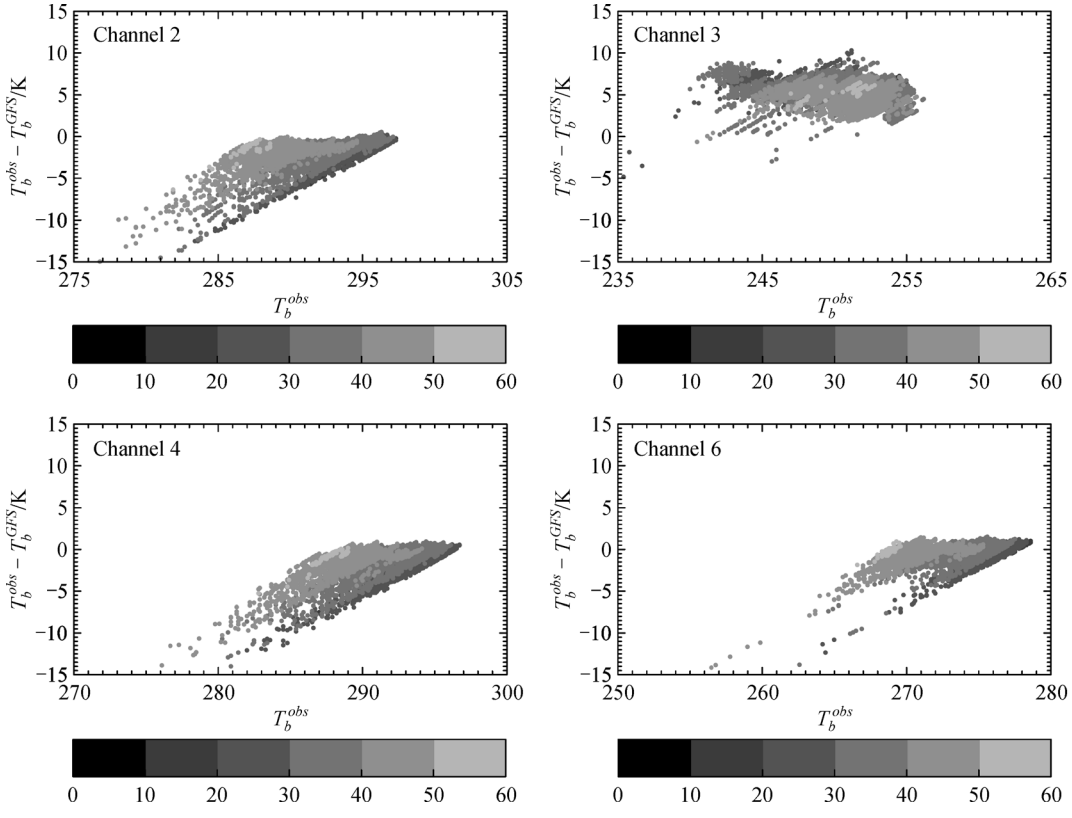

Fig. 9 The dependence of $(T_b^{obs} - T_b^{sim})$ on observed brightness temperature (Unit: K) for GOES-15 channels 2, 3, 4, and 6 when using the GFS analysis as the background.

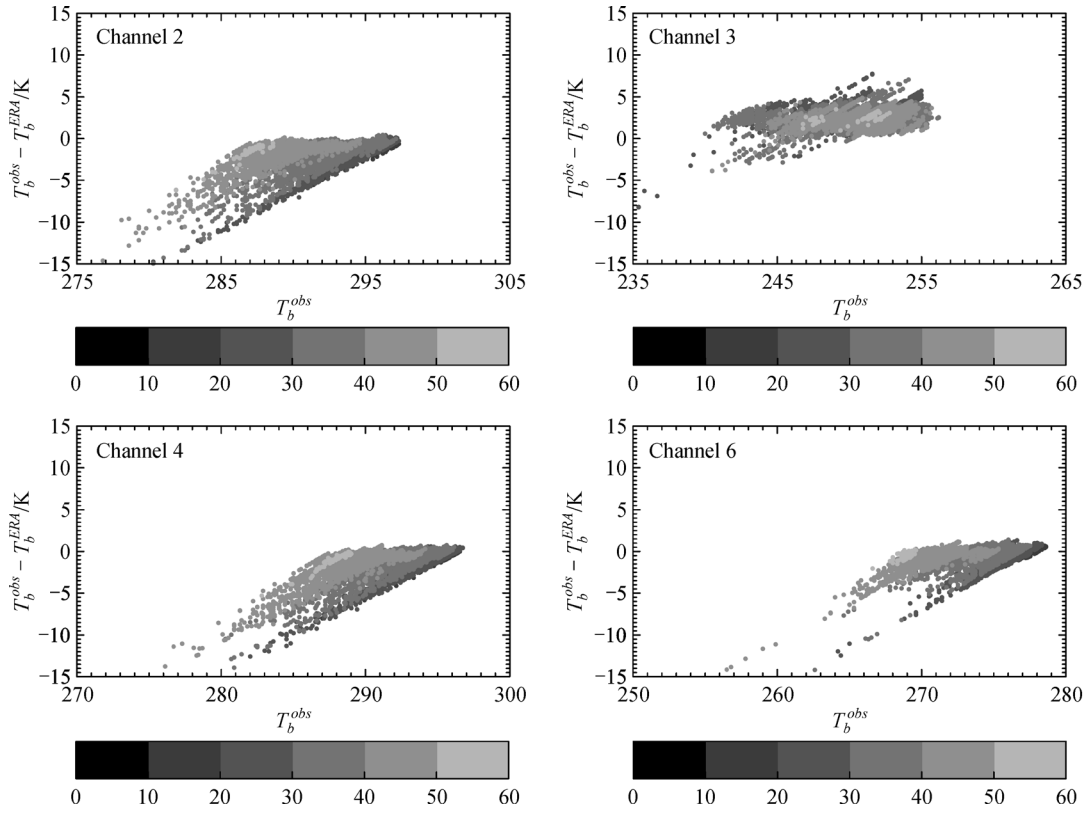

Fig. 10 The dependence of $(T_b^{obs} - T_b^{sim})$ on observed brightness temperature (Unit: K) for GOES-15 channels 2, 3, 4, and 6 when using the ERA-Interim reanalysis as the background.

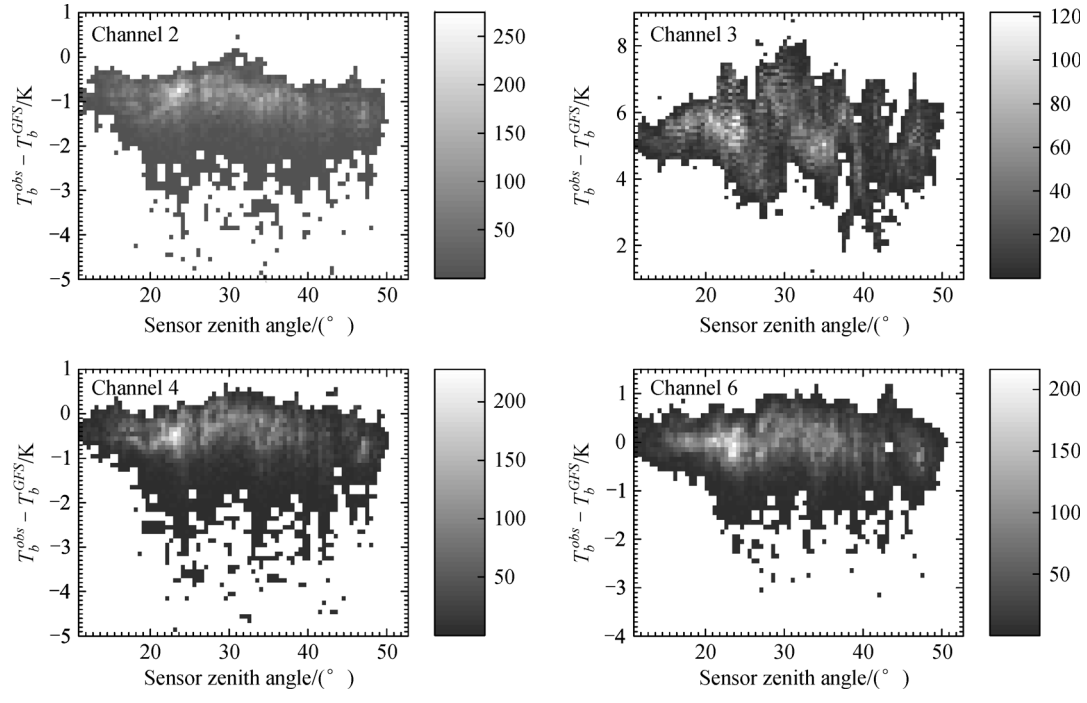

Fig. 11 The dependence of $(T_b^{obs} - T_b^{sim})$ on sensor zenith angle (Unit: degree) for GOES-15 channels 2, 3, 4, and 6 when using the GFS analysis as the background. Colors show the number of observations.

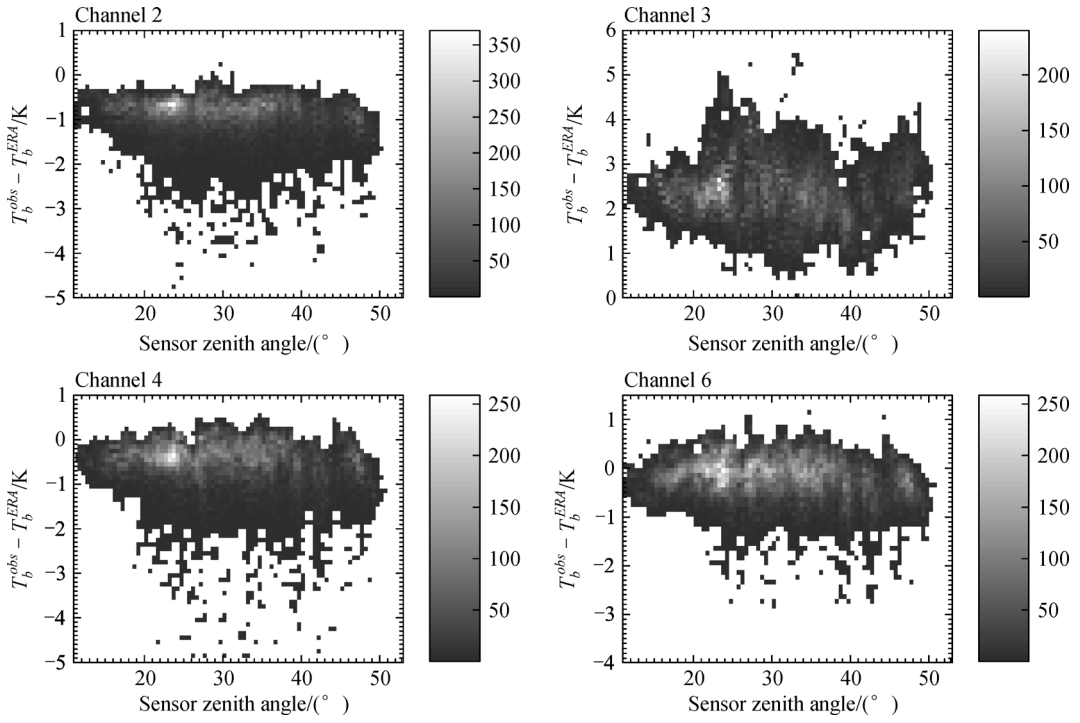

Fig. 12 The dependence of ($T_b^{obs} - T_b^{sim}$) on sensor zenith angle (Unit: degree) for GOES-15 channels 2, 3, 4, and 6 when using the ERA-Interim reanalysis as the background. Colors show the number of observations.

fractions. The GFS analysis and ERA-Interim reanalysis are utilized as input to the CRTM. The numerical results indicate that biases of three infrared surface channels are of magnitudes below 1 K, whereas bias of the infrared water vapor channel can reach up to 5.5 K using GFS analysis and 2.5 K using ERA-Interim reanalysis. Dependencies of biases on scene temperature and sensor zenith angles are also explored in this study. The surface channels 2, 4, and 6 show positive dependencies on scene temperature, whereas the water vapor channel 3 is independent of scene temperature. On the other hand, three surface channels show weak dependence on sensor zenith angle using two datasets, whereas the water vapor channel is heavily dependent on sensor zenith angle using GFS analysis. This indicates potential biases in the GFS water vapor profiles.

The calibration method in this study could not distinguish the instrument biases from the model biases. If large biases exist in the radiative transfer model and background state, the instrumental biases cannot be estimated accurately. As the biases might exist in GFS water vapor profiles, the estimated bias of the GOES water vapor channel is not convincing using GFS analysis. Both NWP fields contain the large biases in their water vapor profiles, but the ERA-Interim reanalysis contains the smaller bias compared to the GFS analysis.

Acknowledgements The author thanks the University of Michigan for providing excellent experimental facilities.

References

Auligné T, McNally A P, Dee D P (2007). Adaptive bias correction for satellite data in a numerical weather prediction system. Q J R Meteorol Soc, 133(624): 631–642

Capderou M (2005). Satellites: Orbits and Missions. Berlin: Springer, 364

Chen Y, Han Y, van Delst P, Weng F (2013). Assessment of shortwave infrared sea surface reflection and nonlocal thermodynamic equilibrium effects in the community radiative transfer model using IASI data. J Atmos Ocean Technol, 30(9): 2152–2160

Cox C, Munk W (1954). Measurements of the roughness of the sea surface from photographs of the sun's glitter. J Opt Soc Am, 44(11): 838–850

Da C (2015). Preliminary Assessment of the Advanced Himawari Imager (AHI) Measurement onboard Himawari-8 Geostationary Satellite. Remote Sens Lett, 6(8): 637–646

Da C, Zou X (2014). An introduction to GOES imager data. Advances in Met S&T, doi: 10.3969/j.issn.2095-1973.2014.04.009

Dee D P (2005). Bias and data assimilation. Q J R Meteorol Soc, 131 (613): 3323–3343

Han Y, Weng F, Liu Q, van Delst P (2007). A fast radiative transfer model for SSMIS upper atmosphere sounding channels. J Geophys Res, 112(D11): 121

Hewison T J, Wu X, Yu F, Tahara Y, Hu X, Kim D, Koenig M (2013). GSICS inter-calibration of infrared channels of geostationary imagers using Metop/IASI. IEEE Trans Geosci Rem Sens, 51(3): 1160–1170

Köpken C, Kelly G, Thépaut J N (2004). Assimilation of meteosat radiance data within the 4D‐var system at ECMWF: assimilation experiments and forecast impact. Q J R Meteorol Soc, 130(601): 2277–2292

Menzel P, Schmetz J, Nieman S, van de Berg L, Gaertner V, Schmit T (1993). Intercomparison of the Operational Calibration of GOES-7 and Meteosat-3/4. US Department of Commerce, National Oceanic and Atmospheric Administration, National Environmental Satellite, Data, and Information Service

Qin Z, Zou X, Weng F (2013). Evaluating added benefits of assimilating GOES imager radiance data in GSI for coastal QPFs. Mon Weather Rev, 141(1): 75–92

Schmit T, Gunshor M, Fu G, Rink T, Bah K (2012). GOES-R Advanced Baseline Imager (ABI) algorithm theoretical basis document for cloud and moisture imagery product (CMIP), Version 3.0

Su X, Derber J C, Jung J A, Tahara Y (2003). The usage of GOES imager clear sky brightness temperatures in the NCEP global data assimilation system. Preprints, 12th Conf. On Satellite Meteorology and Oceanography, Long Beach, CA, American Meteorological Society

Szyndel M D E, Kelly G, Thépaut J N (2005). Evaluation of potential benefit of assimilation of SEVIRI water vapour radiance data from Meteosat‐8 into global numerical weather prediction analyses. Atmos Sci Lett, 6(2): 105–111

Weinreb M, Jamieson M, Fulton N, Chen Y, Johnson J X, Bremer J, Smith C, Baucom J (1997). Operational calibration of geostationary operational environmental Satellite-8 and -9 imagers and sounders. Appl Opt, 36(27): 6895–6904